JOURNAL OF MATERIALS SCIENCE 29 (1994) 2648–2654

Some aspects of electron beam welded and laser welded ferritic Fe–22Cr–3Mo–5Ni–0.3Ru alloy

SIE-CHIN TJONG
Department of Physics and Materials Science, City Polytechnic of Hong Kong, 83 Tat Chee Avenue, Kowloon, Hong Kong

JIN-SON KU, NEW-JIN HO
Institute of Materials Science and Engineering, National Sun-Yat-Sen University, Kaohsiung, Taiwan

Ferritic Fe–22Cr–3Mo–5Ni–0.3Ru alloy was welded by electron beam (EB) and laser techniques. Tensile tests, impact tests, oxalic acid etch, electrochemical potentiokinetic reactivation (EPR) and potential–time measurements were employed to investigate the mechanical properties, microstructural features and corrosion behaviour of the EB and laser welded metals. The oxalic acid etch tests revealed that the microstructure of the EB and laser welded metals consisted of columnar grains and cells, respectively. These structures were formed directly from the substrate by epitaxial solidification. Furthermore, the oxalic acid tests also showed that the EB and laser welded metals were immune to intergranular corrosion. Similar results were obtained by double loop EPR tests.

1. Introduction

Ferritic stainless steels offer certain attractive properties compared to austenitic grades. The ferritics alloys are generally resistant to stress corrosion cracking and localized corrosion, but are not resistant to hydrogen induced cracking. The pitting corrosion resistance of ferritic stainless steels depends significantly on the Cr and Mo contents. However, the ferritic alloys exhibit low fracture toughness and poor weldability, which limit their usage in industrial applications. It is well recognized that the toughness of ferritic alloys can be improved by reducing the carbon and nitrogen levels [1] or by the addition of stabilizing elements such as titanium and niobium [2]. Recent advances in steel-making process have permitted the development of superferritic steels with very low carbon and nitrogen contents. These low interstitial ferritic alloys have been used extensively in the petrochemical industries.

Poor weldability of the ferritic stainless steels is due to the absence of phase transformations, which leads to ferrite grain growth in the heat-affected zone (HAZ). Chromium carbide or nitride precipitation is likely to occur in the HAZ during welding, as the diffusion rate of carbon and nitrogen is very rapid in ferrite. Moreover, atmospheric contamination during conventional arc-welding processes can also result in the embrittlement of weld joints. Inert gas shielded-welding is recommended to minimize contamination of the weld region, as a high degree of cleanliness is essential for welding of superferritic steels. Furthermore, the influence of dissimilar metal fillers on mechanical and corrosion properties are relatively complicated [3]. On the other hand, electron beam (EB) and laser welding are particularly well suited to ferritic alloys because the heat input is much lower than in arc-welding processes. Consequently, ferrite grain growth in the HAZ is restricted. In the welding process, the base alloy is irradiated with a high energy beam causing rapid melting and solidification within a localized region. Such rapid solidification tends to prevent sensitization of the ferritic alloys. As EB and laser welding do not require the use of filler metals, the fusion zone and HAZ are extremely narrow. Moreover, embrittlement due to atmospheric contamination can be avoided in EB welding because the welds must be made under vacuum.

Ferritic stainless steels owe their corrosion resistance in oxidizing aqueous solutions mainly to the formation of passive films on their surfaces. However, the Fe–Cr alloys are active and exhibit high corrosion rates in non-oxidizing hydrochloric and sulphuric acids. It is known that the corrosion resistance of Fe–Cr alloys in non-oxidizing acids can be improved by the addition of small amounts of platinum group metals (PGMs), e.g. Pt, Pd and Ru. The PGM additions tend to cause spontaneous passivism of Fe–Cr alloys in non-oxidizing acids. The improved corrosion resistance results from the enrichment of PGMS on the alloy surfaces during the initial period of active dissolution, and a subsequent potential shift from the active to passive region. It has been reported that the Fe–Cr alloys containing 40 wt % Cr and 0.2 wt % Pd

0022–2461

exhibited self-passivation behaviour and excellent corrosion resistance in boiling sulphuric acid solutions of up to 50% concentration [4]. The Fe–40Cr–0.2Pd alloy has superior corrosion resistance to the Hastelloy alloys grade A, B and C [4]. Tjong and co-workers [5–12] have extensively studied the aqueous corrosion and gaseous oxidation behaviour of ferritic alloys containing PGMs. Tjong reported that the effectiveness of various PGM additions to Fe–40Cr alloys in promoting spontaneous passivation in hydrochloric and sulphuric acid solutions decreases in the order: Pt, Ru, Pd on the basis of electrochemical and surface analytical measurements [9]. However, addition of 40 wt % Cr to Fe-base alloys tends to decrease their impact toughness [1]. Furthermore, Pt, Pd and Cr are expensive alloying elements, and Cr in particular is considered to be a strategic element for some countries. It is necessary to reduce the Cr content of Fe–40Cr alloy to lower levels by partial substitution of Cr with other alloying elements such as Mo. As Ru is the cheapest alloying element among the PGMs, a small amount of Ru is added to Fe–Cr–Mo alloys to improve their corrosive resistance in reducing acids. In this context, Streicher [13] indicated that Ru alloying is more effective than Pt or Pd in increasing the pitting resistance of Fe–28Cr–4Mo alloys in halide media. Recently, Tjong reported that the addition of 0.3% Ru to an Fe–22Cr–3Mo–5Ni ferritic alloy significantly decreases the dissolution rate in boiling 0.5 M HCl solutions [6]. The purpose of this paper is to investigate the mechanical, corrosion and microstructural features of EB welded and laser welded ferritic Fe–22Cr–3Mo–5Ni–0.3Ru alloys. The composition studied (Fe–22Cr–5Ni–3Mo) is close to that of a commercial duplex stainless steel. However, the commercial steel contains approximately 0.2% nitrogen, which yields sufficient austenite stabilization so that a duplex structure results. The alloy used in the present work contained no nitrogen and was fully ferritic.

2. Experimental procedure

The alloy investigated was prepared in a vacuum induction furnace, followed by ingot casting and hot rolling. The chemical composition of the alloy studied is listed in Table I. Nickel is added to the alloy to increase its resistance in reducing acids [14] and to improve impact toughness. The plates were annealed at 820 °C for 1/2 h and subsequently quenched in water.

The solution-treated alloy was welded with a 3 kW (Torvac CVE63B) EB welder. Full penetration welds were made in 7 mm thick plates by a close-square butt-joint technique with the following parameters: potential, 60 kV; current, 42 mA; welding speed, 20 mm s^{-1}; chamber pressure, 2.6×10^{-2} Pa. The solution-treated plates were also welded with a 3 kW (PRC FH-3000) CO_2 laser. Owing to the limited power of the laser facility, the weld run was made from opposite sides to achieve complete penetration. The beam was focused at 2 mm below the work-piece surface. The following welding parameters were employed: laser power, 2.5 kW; welding speed, 10 mm s^{-1}; shielding gas, helium.

TABLE I Chemical composition (wt %) of the alloy investigated

C	N	Cr	Mo	Ni	Ru	Fe
< 0.01	< 0.002	22.3	2.69	5.11	0.3	Balance

Axial rectangular tension specimens of 25 mm gauge length were machined from the solution-treated plates, with their lengths parallel to the rolling direction. Specimens of identical dimension were also prepared from EB and laser welded plates, with the weld metals located in the central portion of the gauge length and transverse to the specimen axis. Charpy impact specimens ($10 \times 55 \times 6$ mm^3) were cut from the solution-treated, EB welded and laser welded plates, respectively. For the welded specimens, the notches were located in the weld metals. The fracture surfaces of impact and tensile specimens were examined in a scanning electron microscope (SEM) Jeol model JSM-820, equipped with a Link AN/85S energy dispersive spectroscopy (EDX) system.

For the electrochemical potentiokinetic reactivation (EPR) test, the specimens were immersed in deaerated 0.5 M H_2SO_4 + 0.01 M KSCN solution at 23 °C. The glass test cell consisted of a working electrode, graphite rod counter electrodes and a saturated calomel reference electrode (SCE). The welded and isothermally heat treated specimens were subjected to EPR testing. The working electrode was ground with SiC paper down to 800 grit, and subsequently polished down to 1 μm diamond. The polished specimen was then immersed in the test cell for 5 min to determine the corrosion potential. It was then polarized anodically to a potential of 300 mV in the passive range, at 2 mV s^{-1}, by using a Princeton Applied Research (PAR) model 273 potentiostat. When this potential was reached, the scanning direction was reversed toward the corrosion potential. The current densities generated during activation (I_a) and reactivation (I_r) were measured. The degree of sensitization is expressed in terms of the I_r:I_a ratio. In addition to the EPR test, the specimens were also electrolytically etched in 10% oxalic acid in order to examine the degree of sensitization exhibited by EB and laser weldments. After oxalic acid etch tests, the specimens were observed in an optical microscope.

Potential–time response measurements were performed in a nitrogen-purged 0.5 M HCl solution at 22 °C. The EB and laser welded samples were polished down to 1 μm diamond. They were placed inside the glass test cell and were then cathodically reduced in 0.5 M HCl solution at − 800 mV (SCE) for 5 min by the potentiostat, in order to remove the oxide formed in air. After cathodic reduction, the specimens were allowed to spontaneously passivate. The change of potential with time was recorded.

3. Results

Fig. 1a shows typical macrostructure of the EB weldment; the microstructure of this weldment is shown in

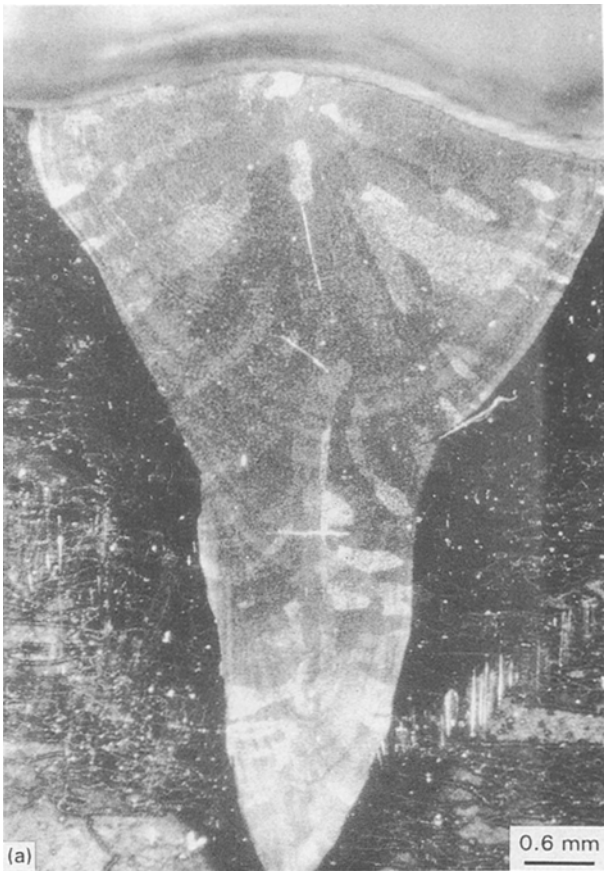

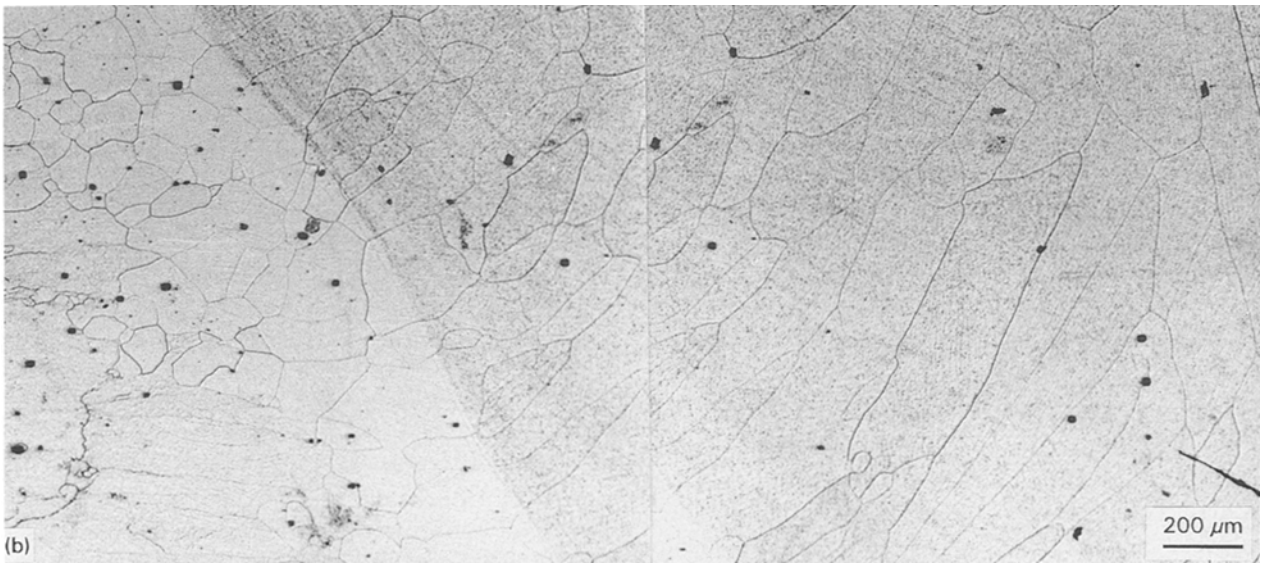

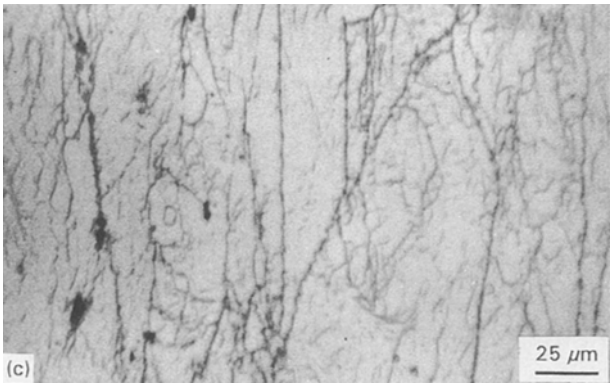

Figure 1 (a) Typical macrostructure of an EB weldment; (b) microstructure of this weldment, and (c) a higher magnification of weld metal after oxalic acid etch test.

Fig. 1b. A higher magnification of the weld metal is shown in Fig. 1c. It is apparent in Fig. 1b that the columnar dendrites that formed in the weld metal were derived from the HAZ grains. During resolidification of an EB weldment, molten metal is brought in contact with the cool substrate. Thus, solidification of the melt occurs epitaxially as the liquid solidifies from its own substrate. Such epitaxial growth has been observed in the EB fusion zone of a single Fe–15Ni–15Cr crystal [15].

Fig. 2 shows the typical microstructure of the laser weldment taken from a longitudinal section. The optical micrograph indicates that the microstructure of the laser weld metal consists predominantly of cellular structure formed by epitaxial solidification, i.e. the cells grow from favourably oriented grains of the base metal. However, a thin planar zone is found along the fusion line.

The results of tension tests on the base, EB and laser welded samples are tabulated in Table II. It is apparent from this table that there is only a small reduction in ductility (percentage elongation) of the EB and laser samples when compared to that of the base metal. The SEM fractograph of the Fe–22Cr–3Mo–5Ni–0.3Ru base alloy after tension test is shown in Fig. 3. One can see that the fracture surface exhibits ductile dimples which form by the microvoid coalescence mechanism and facets associated with quasi-cleavage fracture. This alloy has an average ASTM grain size number of 4–5 when annealed at 820 °C for 30 min. However, brittle cleavage failure is observed when this alloy is annealed at 1100 °C for 1 h due to the coarsening of ferritic grains. For the EB and laser welded Fe–22Cr–3Ni–5Mo–0.3Ru samples, fracture occurred essentially in the base metal. Thus, the fracture surface of welded samples exhibit a similar mixed-dimple and faceted appearance.

The Charpy impact energy of the solution-treated, EB and laser welded Fe–22Cr–3Mo–4Ni–0.3Ru alloys tested at various temperatures are listed in Table

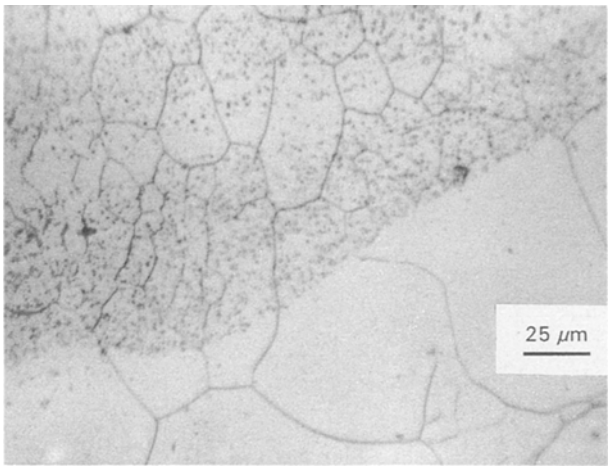

Figure 2 Microstructure of the laser welded Fe–22Cr–3Mo–5Ni–0.3Ru alloy (oxalic acid etch).

TABLE II Tensile properties of solution treated, EB welded and laser welded Fe–22Cr–3Mo–5Ni–0.3Ru alloy

Material condition	0.2% offset yield strength (MPa)	Elongation (%)
Annealed	559	22
EB welded	548	19
Laser welded	540	18

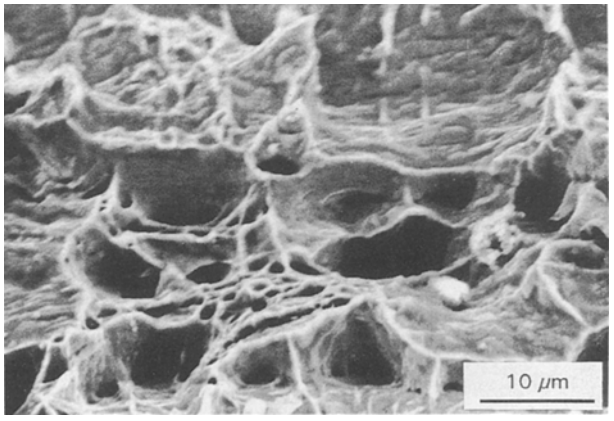

Figure 3 SEM fractograph of the Fe–22Cr–3Mo–5Ni–0.3Ru base alloy after tensile tests.

III. Moreover, it is possible to examine the fracture surface of the EB and laser fusion zone as the notches are located in the weld metals. Fig 4 shows a typical SEM fractograph of the base metal after impact testing at 23 °C. This fractograph reveals that cleavage is the predominant fracture mode and is accompanied by a small amount of dimples. This can be expected as the notchs of the impact specimens increase the tendency for cleavage failure by producing a triaxial tensile state of stress and high local strain hardening. These can lead to ductile dimples as shown in Fig. 3, where it is converted into cleavage fracture. Fig. 5a shows an SEM fractograph of the EB weld metal at low magnification after impact tests at 23 °C. Higher magnification in Fig. 5b shows the fracture path to be associated with the columnar dendritic weld structure. A similar fracture appearance is observed for the laser weldment after impact testing at 23 °C.

TABLE III Charpy impact energy (*J*) of solution-treated, EB welded and laser welded Fe–22Cr–3Mo–5Ni–0.3Ru alloy tested at various temperatures

Material condition	− 196 °C	− 40 °C	23 °C
Annealed	38	60	85
EB welded	23	55	55
Laser welded	26	43	65

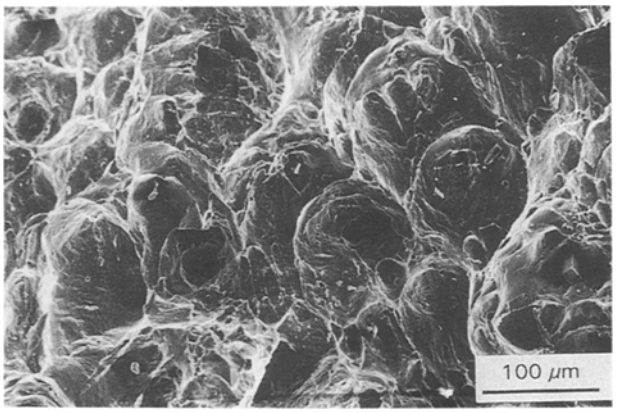

Figure 4 SEM fractograph of the Fe–22Cr–3Mo–5Ni–0.3Ru base alloy after impact tests at 23 °C.

Figs 6 and 7 show the potentiokinetic curves for the base and sensitized alloy specimens exposed to de-aerated 0.5 M H_2SO_4 + 0.01 M KSCN solutions, respectively. The EPR curve for the laser weld metal is shown in Fig. 8. KSCN is a grain boundary activator when the specimen is sensitized. Non-sensitized stainless steels exhibit low current density during the reactivation stage, due to stability of the passive film. However, sensitized stainless steels show high current density due to breakdown of the passive film in chromium depleted areas near grain boundaries. The EPR method was initially developed for type 304 austenitic stainless steel [16], but it has been successfully applied to the ferritic stainless steels [17]. Clarke *et al.* [16] used a single loop EPR method to evaluate the sensitization of stainless steel, i.e. only a reactivation scan is performed after passivating a specimen in de-aerated 0.5 M H_2SO_4 + 0.01 M KSCN at 200 mV (SCE) for 2 min. On the other hand, in the double loop EPR method, the reactivation scan from the potential in the passive state is preceded by an anodic scan from the open circuit potential [18]. The main advantage of the double loop test is that it is not necessary to normalize the I_r or the ratio $I_r:I_a$ with a grain size factor.

Fig. 9 shows the potential–time response curves of the base alloy and laser weld metal in 0.5 M HCl solutions. For the base alloy, the initial potential is located at − 570 mV (SCE), and it is then displaced towards anodic region. It reaches a peak potential of

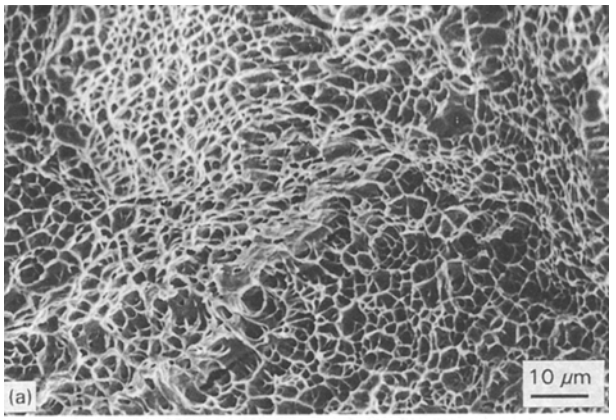

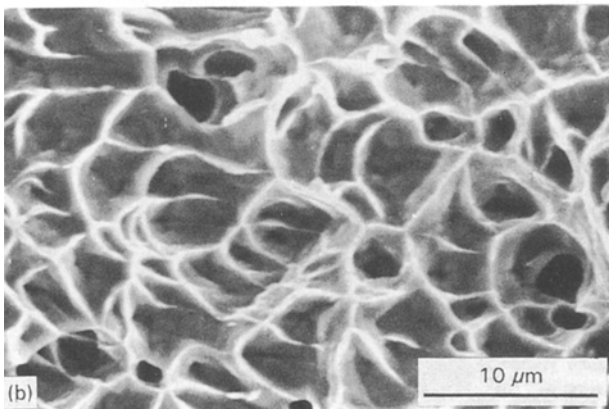

Figure 5 (a) SEM fractograph of the EB welded Fe–22Cr–3Mo–5Ni–0.3Ru alloy after impact tests at 23 °C, and (b) at higher magnification.

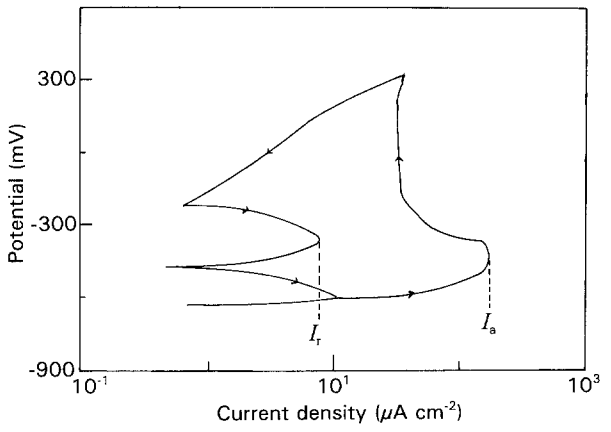

Figure 6 Double loop EPR curve for the base alloy exposed in de-aerated 0.5 M H_2SO_4 + 0.01 M KSCN solutions at 23 °C.

about − 260 mV after 678 s, and then gradually stabilizes at − 381 mV after 2000 s. However, the corrosion potential of laser weld metal is slowly displaced towards − 412 mV after 2000 s. Similar potential–time response behaviour is observed in EB weld metal. The results of EPR tests are listed in Table IV.

4. Discussion

The microstructure of EB weld metal consists mainly of columnar grains formed by epitaxial growth (Fig. 1b). Both crystallographic orientation of the base

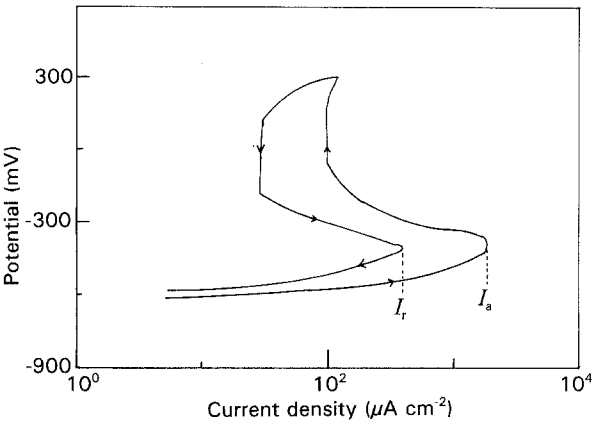

Figure 7 Double loop EPR curve for the Fe–22Cr–3Mo–5Ni–0.3Ru alloy after sensitization treatment at 600 °C for 2 h followed by air cooling.

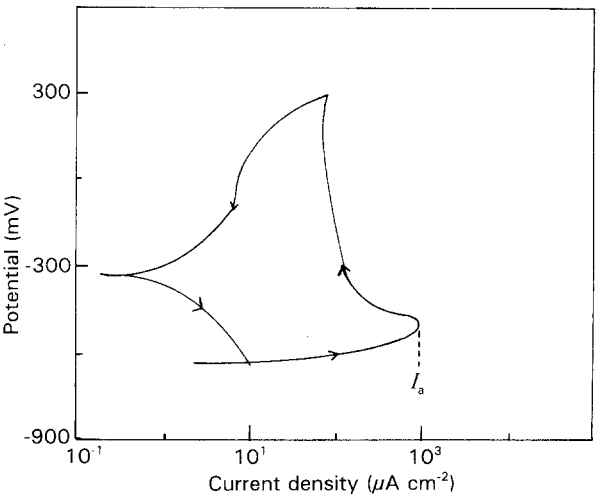

Figure 8 Double loop EPR curve for the laser weld metal exposed in de-aerated 0.5 M H_2SO_4 + 0.01 M KSCN solutions at 23 °C.

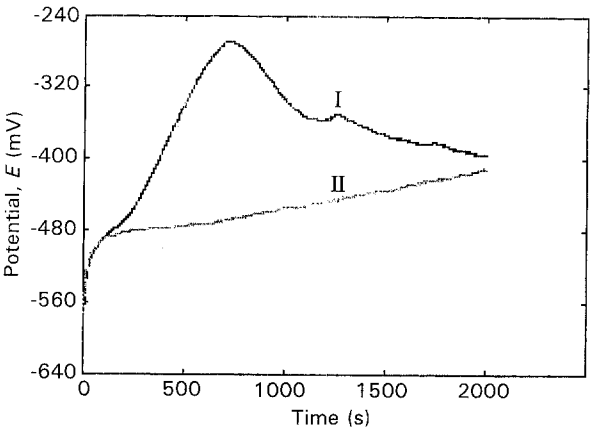

Figure 9 Potential–time response curves of the base alloy, and laser weld metal exposed in 0.5 M HCl solution at 22 °C: (I) base alloy; (II) laser weld metal.

metal grains and the thermal gradient direction can influence the development of weld metal microstructures. In polycrystalline metals, grains in contact with the melt exhibit different crystallographic orientations with respect to the melt–substrate interface.

TABLE IV EPR results for the base alloy, EB and laser weldments

Material condition	I_r ($\mu A\,cm^{-2}$)	I_a ($\mu A\,cm^{-2}$)	$I_r:I_a$
Annealed	9	160	0.056
Sensitized	380	1900	0.200
EB weld metal	0	850	0.000
Laser weld metal	0	900	0.000

Those grains with their crystallographic axes aligned with the flow direction, grew preferentially over those with other orientations. Preferential growth in the heat flow direction subsequently leads to a coarsening of the polycrystalline grains, because those grains with less favourable orientation will be eliminated during the growth process [19]. From this work, one can see that epitaxial solidification also leads to grain coarsening associated with the formation of columnar dendrites (Fig. 1c). It is well known that dendrite formation is related to high cooling rates, alloy content and undercooling. The cooling rates of the electron and laser melt pool are typically in the range of 10^5–$10^8\,K\,s^{-1}$ [20, 21]. Consequently, large undercoolings can be attained in the melt prior to epitaxial solidification, thus favouring a dendritic mode of solidification [22]. On the other hand, from other work on stainless steels that solidify to ferrite, it is virtually impossible to identify dendritic growth; presumably because of high diffusion rates in the solid phase [23]. Kou and Le [24] reported that the dendritic structure was barely visible in a 430 ferritic stainless steel weld quenched with liquid tin during welding.

The formation of cellular structure in the laser weld metal is related to the ratio $G:R$, where G is the temperature gradient in the liquid and R is the solidification rate. High ratio values facilitate planar front growth, whereas low ratio values favour cellular or cellular dendritic growth modes [25]. A particular characteristic of laser welding is that a high value of $G:R$ exists near the melt–substrate interface, which facilitates planar growth. Heat transfer calculations [26] show that the $G:R$ ratio reaches a maximum at the fusion boundary of a laser weld, as a high temperature gradient exists near this region. However, when the liquid–solid interface moves away from the fusion line, G decreases and R increases, thus facilitating cellular growth.

The impact energy of the Fe–22Cr–3Mo–5Ni–0.3Ru base alloy at various test temperatures is considerably higher than that of the EB and laser weld metals. The lower impact energy of the weldments can be correlated with a higher proportion of cleavage failure, as revealed by the SEM fractographs (Fig. 5a,b). These results suggest that resistance to crack initiation during impact loading is quite high for the solution-treated base alloy. However, the presence of long columnar grains and cellular structures in EB and laser weld metals possibly assists greatly in the initiation of brittle cracks at the time of dynamic loading due to solute segregation in this region. Initiation of brittle fracture was, in most cases, associated with the precipitation of carbides or intermetallic compounds in ferritic stainless steels.

The oxalic acid tests reveal no evidence of sensitization in the HAZ of the EB and laser weldments (Fig. 1b and Fig. 2). A step structure, by microscopic examination of the etched surface, indicates a non-sensitized condition; whereas a ditch structure indicates susceptibility to grain boundary attack. The elimination of the ditch structure in the HAZ of the EB and laser weldments indicates an improvement in intergranular corrosion resistance. Damborena *et al.* reported that laser melting is very effective in suppressing the sensitization of type 304 stainless steel [27]. Moreover, embrittlement associated with atmospheric contamination is eliminated due to the very high cooling rates and the use of inert gas shielding in laser welding. The fast cooling produced, limits the time that the weld metal stays in the molten state, thereby reducing pick up of carbon, nitrogen or oxygen.

From Fig. 6, it is apparent that the reactivation curve of solution-treated alloy displays a peak in the range -290 to -580 mV (SCE), which corresponds to reactivation of chromium-depleted grain boundaries. As the diffusion of carbon is so rapid in ferritic stainless steels, even water quenching cannot prevent chromium carbide precipitation. This current density (I_r) increases dramatically for the base alloy sensitized at 600 °C for 2 h followed by air cooling (Fig. 7). On the other hand, no I_r peak can be observed in the reactivation curve of the laser weld metal exposed in de-aerated 0.5 M H_2SO_4 + 0.01 M KSCN solutions (Fig. 8). This can be expected, as rapid cooling and solidification rates during laser welding prevents chromium carbide precipitation. The HAZ is found to have an EPR curve similar to that of the laser weld metal. Furthermore, the EB weldment also exhibits similar reactivation curves to those of the laser weldment.

The effect of Ru addition on the corrosion behaviour Fe–22Cr–3Mo–5Ni alloy exposed in hydrochloric solution is now considered. Addition of 0.3% Ru to the base alloy leads to a shift of the corrosion potential from the region of active dissolution to the passive region (Fig. 9). This is associated with the enrichment of Ru on the alloy surface after cathodic reduction. As Ru is characterized by low overvoltage for hydrogen evolution, it promotes spontaneous passivation of the annealed Fe–22Cr–3Mo–5Ni–0.3Ru alloy in 0.5 M HCl solution. From Fig. 9, a slight shift in the corrosion potential of laser weld metal towards more positive values is mostly associated with the accumulation of Mo and Ni on the weld metal surface. It is generally established that Mo as an alloying element does not only retard the anodic dissolution process [28], but also efficiently enhances the cathodic process by reducing the hydrogen evolution overvoltage [29]. In the case of high chromium steels, Mo gives rise to a slight shift of the corrosion potential towards the anodic region [29]. On the other hand, Ni also facilitates hydrogen evolution, through Ni accumulation on the surface of CrNi steel [14]. However, because of the hydrogen overpotential,

which is higher on Ni than on PGMs, Ni cannot give rise to a potential shift towards more positive values [14]. From the above discussion, a small amount of Ru in the laser weld metal also results in a potential shift towards a more anodic potential of -412 mV after an extended period of 2000 s. It seems likely that the lower corrosion resistance of the laser weld metal in hydrochloric solutions stems from residual segregation, or a change in carbon, oxygen, or nitrogen contents.

5. Conclusions

1. The optical micrographs reveal that columnar grains and cellular structures are formed in the weld metals of EB and laser weldments, respectively, as a result of appropriate $G:R$ conditions.

2. The percentage elongation of the EB and laser weldments is almost comparable to that of the Fe–22Cr–3Mo–5Ni–0.3Ru base alloy. However, the impact toughness of these weldments is considerably lower than that of the base alloy.

3. The EPR and oxalic acid tests reveal that the EB and laser weldments are not susceptible to intergranular corrosion.

4. The annealed Fe–22Cr–3Mo–5Ni–0.3Ru alloy exhibits spontaneous passivation in 0.5 M HCl solution. However, the corrosion potentials of laser and EB weld metals are displaced towards more positive values after extended periods of time when exposed in 0.5 M HCl solutions.

Acknowledgements

The authors would like to thank Mr T. F. Hung for assistance in SEM observations. The alloy investigated was fabricated at Mintek, which is gratefully acknowledged.

References

1. W. D. BINDER and H. R. SPENDELOW Jr, *Trans. Am. Soc. Met.* **43** (1951) 759.
2. H. ABO, T. NAKAZAWA, S. TAKEMURA, M. ONOYAMA, H. OGAWA and H. OKADA, in "Stainless Steel 77", edited by R. Q. Barr (Climax Molybdenum Co., Greenwich, CT, 1977) p. 35.
3. K. F. KRYSIAK in "Toughness of Ferritic Stainless Steels", ASTM STP 706, edited by R. A. Lula (American Society for Testing and Materials, Philadelphia, PA, 1980) p. 221.
4. N. D. TOMASHOV and G. P. CHERNOVA, *Prot. Met. (USSR)* **11** (1975) 379.
5. S. C. TJONG and J. B. MALHERBE, *Appl. Surf. Sci.* **40** (1989) 1.
6. S. C. TJONG, *Werks. Korros.* **40** (1989) 729.
7. *Idem., Appl. Surf. Sci.* **44** (1990) 7.
8. S. C. TJONG and J. B. MALHERBE, *ibid.* **44** (1990) 179.
9. S. C. TJONG, *ibid.* **45** (1990) 301.
10. *Idem., ibid.* **51** (1991) 157.
11. *Idem., ibid.* **55** (1992) 57.
12. S. C. TJONG and C. K. CHUNG, *X-ray Spectrom.* **22** (1993) 172.
13. M. A. STREICHER, *Corrosion* **30** (1974) 77.
14. N. D. TOMASHOV, G. P. CHERNOVA and L. N. VOLKOV, *Prot. Met. (USSR)*, **6** (1970) 388.
15. S. A. DAVID, J. M. VITEK, M. RAPPAZ and L. A. BOATNER, *Met. Trans.* **21A** (1990) 1753.
16. W. L. CLARKE, R. L. COWAN and W. L. WALKER, in "Intergranular Corrosion of Stainless Alloys", ASTM STP 656 (American Society of Testing and Materials, Philadelphia, PA, 1987) p. 99.
17. S. FRANGINI and A. MIGNONE, *Corrosion* **48** (1992) 715.
18. M. AKASHI, T. KAWAMOTO and F. UMEMURA, *Boshoku Gijutsu (Corros. Eng.)* **29** (1980) 163.
19. V. T. SWAMY, S. RANGANATHAN and K. CHATTOPADHYAY, *J. Cryst. Growth* **96** (1989) 628.
20. J. A. BROOKS and A. W. THOMPSON, *Int. Mater. Rev.* **36** (1991) 16.
21. L. S. WEINMAN and J. N. DEVAULT, in "Proceedings of Laser-Solid Interactions and Laser Processing", edited by S. D. Ferres, H. J. Leamy and J. M. Poate (American Institute of Physics, New York, 1978), p. 239.
22. Y. WU, T. J. PICCONE, Y. SHIOHARA and M. C. FLEMINGS, *Met. Trans.* **18A** (1987) 915.
23. Y. KOMIZU, *Met. Con.* **18** (1986) 104R.
24. S. KOU and Y. LE, *Met. Trans.* **13A** (1982) 1144.
25. W. TILLER, K. A. JACKSON, J. W. RUTTER and B. CHALMERS, *Acta Metall.* **1** (1953) 428.
26. J. MAZUMDER and W. M. STEEN, *J. Appl. Phys.* **51** (1980) 941.
27. J. DE DAMBORENA, A. J. VAZQUEZ, J. A. GONZALEZ and D. R. F. WEST, *Surf. Eng.* **5** (1989) 235.
28. E. A. LIZLOVS and A. P. BOND, *J. Electrochem. Soc.* **118** (1971) 22.
29. N. D. TOMASHOV, S. A. GOLOVANENKO, E. A. UL'YANIN, G. P. CHERNOVA and A. D. GORONKOVA, *Prot. Met (USSR)* **16** (1980) 83.

Received 29 April
and accepted 24 November 1993